Cold Cracking Development in AA7050 Direct Chill–Cast Billets under Various Casting Conditions

M. LALPOOR, D.G. ESKIN, and L. KATGERMAN

Cold cracking is a potentially catastrophic phenomenon in direct chill (DC) casting of 7*xxx* series aluminum alloys that leads to safety hazards and loss of production. The relatively low thermal conductivity and wide solidification temperature range in these alloys results in accumulation of residual thermal stress under nonuniform cooling conditions of the billets. In addition, such alloys show a severe loss in ductility below a critical temperature of 573 K (300 °C). This brittleness along with high stress concentration at the tips of voids and microcracks can lead to catastrophic failure. Casting process parameters affect the magnitude and distribution of stresses in the billet and increase the susceptibility of the material to cold cracking. In order to investigate the effect of casting process parameters such as casting speed, billet size, and water flow rate, thermomechanical simulations were applied using ALSIM5 casting simulation software. Among the studied casting process parameters, the increased billet size and high casting speed resulted in the most dramatic increase in residual stress level. Critical crack sizes that led to catastrophic failure were also calculated and are reported against process parameters.

DOI: 10.1007/s11661-010-0256-9

I. INTRODUCTION

DURING the direct chill (DC) casting process, heat extraction occurs from the surface and, to a lesser extent, from the bottom of the ingot. As a result, high-temperature gradients appear facilitated by the direct contact of water or starting block (bottom block) with the partially solidified ingot, as schematically shown in Figure 1. High-temperature gradients lead to inhomogenous contraction and eventually thermal stresses appear as one part of the billet restrains another.[1,2] Sign, magnitude, and distribution of the thermal stresses depend on the thermophysical properties of the alloy under discussion and also on the casting process parameters. Comparison of the thermal properties of various groups of aluminum alloys reveals that 7*xxx* series (*e.g.*, AA7050 and AA7075) have the lowest thermal conductivity, widest solidification temperature range, and relatively higher coefficient of thermal expansion.[3] Combination of such unfavorable thermal properties along with poor ductility in the as-cast condition[4,5] makes such alloys vulnerable to both hot and cold cracking.[6,7] The hot crack or tear is defined as a failure occurring above the solidus of the alloy, in the presence of liquid phase. The cold crack is a failure occurring below the solidus. Casting process parameters such as casting speed[8–10] and water flow rate[10] can affect the stress level in the ingot and enhance the problem. Size and geometry of the ingot influence the thermal stress level and play an important role in crack susceptibility.[1,11] Even the shape of the bottom block (Figure 1) controls the state of thermal stresses in the start up phase and can result in distortion of the ingot bottom (butt curl) or formation of surface cracks.[12,13] In spite of all modifications and some technical approaches to prevent cold cracking,[7,14,15] it still remains a major problem in DC casting of high-strength aluminum alloys.

Thermomechanical simulations of the DC-casting process have been used extensively for optimization of the cast production line and minimizing the occurrence of ingot cracking without conducting expensive experimental trials.[16] Simulation results can reveal the state of residual stresses and indicate the critical locations where maximum normal stress appears.[6,16–19] At the same time, application of fracture mechanics to the problem using the maximum principal stress component has revealed the critical crack/defect size leading to catastrophic failure.[20,21] The reliability of the simulated stresses, however, depends on how close the constitutive parameters and mechanical properties used in the simulation are to the actual material properties. In our previous article,[22] we used the constitutive parameters and plane strain fracture toughness (K_{Ic}) values of the genuine as-cast material for simulation of residual stresses in the DC-cast billet. The next step taken in the current article is to study the influence of casting variables on magnitude and distribution of residual thermal stresses in DC-cast billets. Ever increasing demand of the industry for higher productivity rates, on the one hand, and complaints on unsuccessful casting trails with newly developed high-strength aluminum alloys, on the other hand, necessitate the systematic

M. LALPOOR, Postdoctoral Researcher, is with the Materials Innovation Institute, 2628 CD Delft, The Netherlands. Contact e-mail: mlalpoor@gmail.com D.G. ESKIN, Fellow M2i, Materials Innovation Institute, is Associate Professor, Department of Materials Science and Engineering, Delft University of Technology. L. KATGERMAN, Professor, is with the Department of Materials Science and Engineering, Delft University of Technology, 2628 CD, Delft, The Netherlands.
Manuscript submitted October 29, 2009.
Article published online June 11, 2010

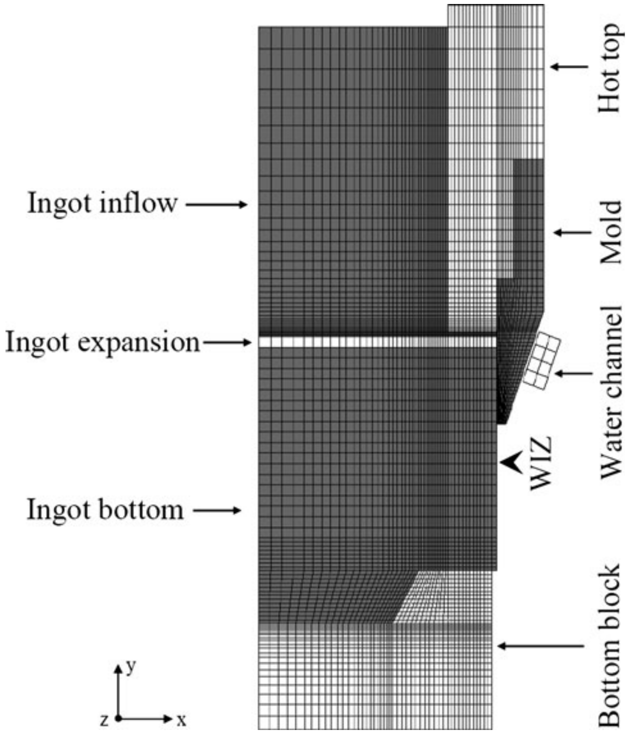

Fig. 1—Geometry of the DC-cast billet used for simulations showing the hot top, mold, bottom block, and the casting aluminum part consisting of cast top, cast expansion, and cast bottom. Approximate position of the water impingement zone (WIZ) is also indicated on the billet surface.

study of the effect of casting variables on cracking susceptibility of billets.

In this research work, the finite element package ALSIM5* has been used to investigate the effect of casting variables including casting speed, billet size, water temperature, water flow rate, melt temperature, and casting time on the magnitude and distribution of residual thermal stresses in DC-cast AA7050 billets. The ALSIM software is used in computer simulation of DC casting and has been described in detail elsewhere.[18,23–26] Having detected the most influential variables, corresponding critical crack sizes were calculated for the most critical locations of the billet using the maximum principal stress values. The results reported in this article can be applied for optimization and improvement of the casting production line in aluminum industry and may lead to production of crack-free billets.

*ALSIM is a casting-simulation software developed by the Norwegian Institute for Energy Technology (IFE), Kjeller, Norway.

II. MODEL SETUP

ALSIM5 was used for the computation of temperature profile and stress/strain fields for round AA7050 billets under various casting conditions. A detailed description of the models involved can be found elsewhere.[23–26] The simulated geometry consisted of the hot top, mold, water jet, bottom block, and the casting domain, as shown in Figure 1. Two-dimensional rectangular elements were used that become finer on moving from the center toward the surface of the billet (Figure 1). As the bottom block moves downward during casting, new elements with size of 0.75 mm are added to the geometry at the casting speed to simulate continuous casting conditions. Meanwhile, the mold, hot top, and molten metal retain their initial position. Simulations were run in two dimensions, and due to axial symmetry, only half of the billet was considered. Time-dependent thermal boundary conditions are defined to account for filling time, air gap formation between the billet and the bottom block as well as at the billet surface, and for different heat extraction in different parts of the casting system.[18] The standard process parameters are listed in Table I. Casting speed, billet size, water temperature, water flow rate, casting time, and melt temperature were varied according to the values in Table II. In the case of changing water temperature, water flow rate, melt temperature, or casting time conditions, other parameters were kept the same as standard ones, as indicated in Table I. For higher casting speeds and larger billet diameters, however, water flow rates were increased accordingly to compensate for the higher heat input related to the greater mass of hot metal coming into the mold.

Table I. Description of Standard Casting Process Parameters

Process Parameter	Value
Ingot diameter (mm)	200
Final length of the billet (mm)	500
Casting speed (mm/s)	1
Melt temperature (°C)	680
Water flow rate (L/min)	80
Water temperature (°C)	15
Start temperature of bottom block (°C)	20

Table II. Selected Cast Variables and Their Values

Process Parameter	Value
Ingot diameter (mm)	200, 300, and 400
Final length of the billet (mm)	500, 1000
Casting speed (mm/s)	1, 1.5 and 2
Melt temperature (°C)	680 and 700
Water flow rate (L/min)	40, 80, and 120
Water temperature (°C)	15, 25, and 45

Chemical composition of the tested alloy is listed in Table III. Thermal as well as physical properties of the alloy were obtained from the thermodynamic database JMat-Pro (Sente Software Ltd., Surrey, United Kingdom) provided by Corus–Netherlands (IJmuiden) and are shown in Table IV. The liquidus and nonequilibrium solidus were determined through differential scanning calorimetry tests for the grain-refined alloy as 905 K (632 °C) and 735 K (462 °C), respectively. The fraction liquid in the solidification range between the liquidus and the nonequilibrium solidus was calculated by the Scheil equation (JMat-Pro), and results are shown in Table V. In ALSIM5, the latent heat of solidification is included in the enthalpy and is released as enthalpy is reduced due to cooling.[27] Mechanical properties and constitutive parameters of the grain-refined alloy have been measured by authors in the genuine as-cast condition (Table VI), and the details may be found elsewhere.[22,28] Mechanical behavior of the material at high temperatures is different in different temperature ranges. Therefore, different models are used to describe this behavior, and some characteristic temperatures define the boundaries between them. An extended Ludwik equation[29] and ALSPEN equations[18] were used to simulate the viscoplastic behavior of the material below the onset temperature of strain hardening 663 K (390 °C).[18] Between this temperature and the so-called merge-properties temperature, low-temperature strain hardening equations (Ludwik and ALSPEN) are merged with the mushy zone equations (cohesion model),[30] and details on the models may be found elsewhere.[31] The merge-properties temperature is defined to be a few degrees below the solidus 728 K (455 °C). Between the merge-properties temperature and rigidity temperature (onset of thermal contraction in the mushy zone, 832 K (559 °C), which was measured experimentally by authors using the solidification contraction setup[32]), the cohesion model[30] was used to simulate the thermomechanical behavior of the material in the mushy zone. As the rheological parameters of the 7050 alloy are not available in the literature, the rheological parameters of the Al-2 wt pct Cu were used instead.[33]

III. SIMULATION RESULTS

Figure 2 shows the distribution of residual thermal stresses in a 7050 DC-cast billet with the diameter of

Table III. Chemical Composition of the 7050 Alloy Used for Simulations

Alloying Elements, Wt Pct									
Zn	Mg	Cu	Zr	Cr	Mn	Ti	Fe	Si	Al
6.3	2.42	2.49	0.098	<0.01	0.04	0.03	0.07	0.04	balance

Table IV. Thermal Properties of the 7050 Alloy Used for Simulations (JMat-Pro)

Temperature K (°C)	Density (kg/m^3)	Thermal Conductivity (W/m·K)	Coefficient of Thermal Expansion (10^{-5}/K)	Specific Heat (J/kg·K)
293 (20)	2825.8	149.4	2.29	857
373 (100)	2811.0	156.0	2.45	897
473 (200)	2790.1	162.7	2.67	939
573 (300)	2767.8	168.2	2.88	979
673 (400)	2744.1	173.0	3.10	1020
773 (500)	2699.8	160.9	3.45	1373
873 (600)	2629.9	124.5	4.03	4125
905 (632)	2515.0	80.8	4.88	1115
973 (700)	2491.6	83.2	5.11	1141

Latent heat of fusion (at 734 K (461 °C)) = $376.14 \cdot 10^3$ J/kg.

Table V. Fraction Liquid Gained from Scheil Equation (JMat-Pro)

Temperature K (°C)	905 (632)	904 (631)	903 (630)	898 (625)	893 (620)	883 (610)	873 (600)	853 (580)	813 (540)	773 (500)	733 (460)
f_l	1	0.97	0.94	0.78	0.65	0.49	0.38	0.27	0.16	0.12	0

Table VI. Constitutive Parameters and Mechanical Properties of the 7050 Alloy; Poisson's Ratios (JMat-Pro) are Also Shown*

Temperature K (°C)	K (MPa)	n	m	E (GPa)	Poisson's Ratio
293 (20)	774 ± 32	0.42 ± 0.02	0	67.9	0.338
373 (100)	626 ± 13	0.38 ± 0.01	0	64.9	0.341
473 (200)	392 ± 11	0.21 ± 0.006	0	61.2	0.346
573 (300)	199 ± 4.5	0.11 ± 0.007	0.03 ± 0.007	57.4	0.352
673 (400)	174 ± 5	0.09 ± 0.01	0.15 ± 0.009	53.6	0.358

*K is the consistency of the alloy (stress at $\varepsilon = 1$ and $\dot{\varepsilon} = 1\ s^{-1}$), n is the strain hardening coefficient, and m is the strain rate sensitivity in the extended Ludwik equation.[29] E is the Young's Modulus.

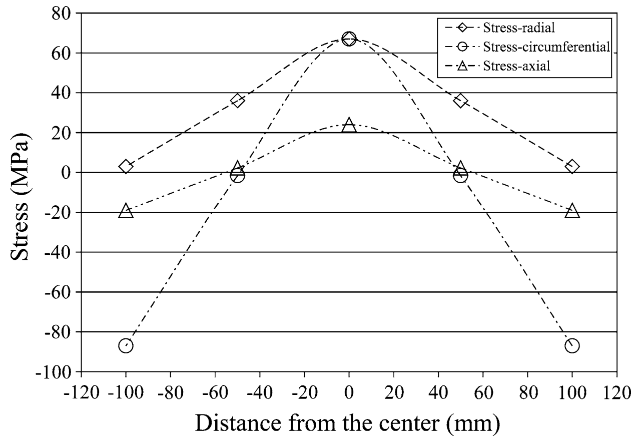

Fig. 2—Distribution of residual thermal stresses (radial, circumferential, and axial) in the lower part of a 7050 DC-cast billet after 1000 s of casting (200-mm diameter and 1-mm/s cast speed).

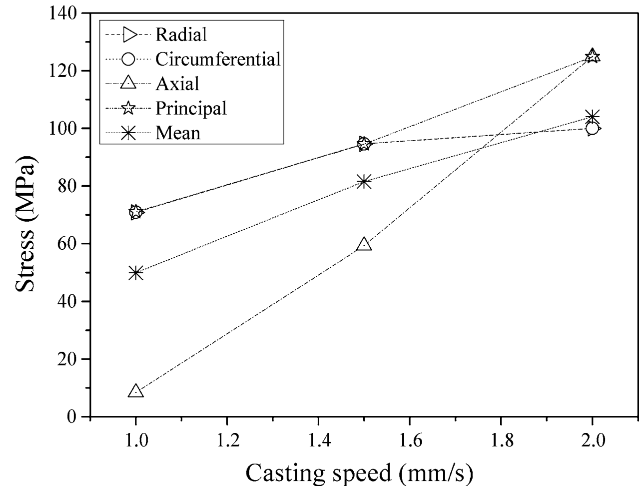

Fig. 3—Effect of cast speed on residual stress values formed in the center of the billet with the diameter 200 mm. Radial, circumferential, axial, maximum principal, and mean stresses are reported in this figure.

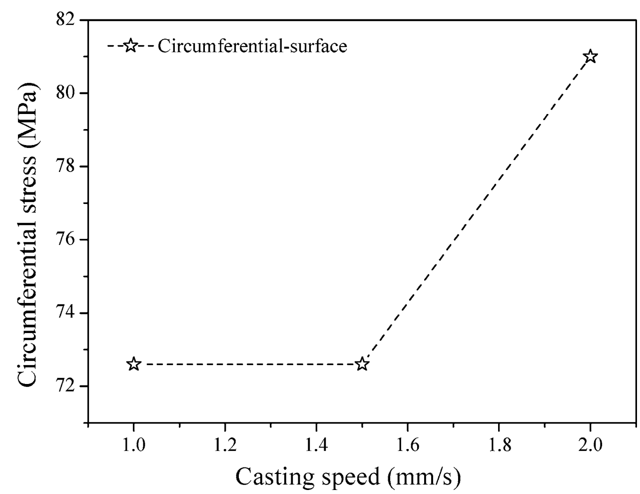

Fig. 4—Circumferential (maximum principal) stress values *vs* cast speed in the WIZ at the surface of the billet with the diameter 200 mm.

200 mm after 500 seconds of standard casting (Table I). The selected points have the following coordinates (Figure 1): surface (x: 95 mm, y: 65 mm), midradius (x: 48 mm, y: 65 mm), and center (x: 1×10^{-5} mm, y: 65 mm), with coordinate point in the center of the top surface of the bottom block. As can be seen in all radial (rr), circumferential ($\theta\theta$), and axial (zz; y in Figure 1) directions, the stresses appear to be tensile in the center, and by moving to the surface, they diminish or turn to compressive. For more details of stress evolution and contour maps of the stress components, one may refer to the previous articles.[22,34] Investigation of the simulation results showed that water temperature, water flow rate, and cast temperature had no noticeable effect on the state of residual thermal stresses. The threshold water flow rate of 80 L/min was found to be sufficient to prevent the remelting of the solidified shell at the surface of the billet (bleed-out) in the standard case. Although lower stresses were recorded at the lower water flow rates, the bleed-out may make the experimental casting trial impossible. Higher amounts of water flow rate did not have any impact on the results either. The casting speed and billet size, however, appeared to be the most influential variables. Figure 3 shows the effect of casting speed on the magnitude of various stress components as well as the mean (hydrostatic) stress in the center of the billet. The largest tensile stress appeared in the center in radial, circumferential, and axial directions (Figure 3) and at the surface in the water impingement zone (WIZ, Figure 1) in the circumferential direction (Figure 4). Stresses reported here correspond to the casting time t = 200 seconds (1 and 1.5 mm/s) and t = 275 seconds (2 mm/s) at which the maximum principal stress appears in the center of the billet. In the WIZ, however, the maximum principal stress is reached after roughly 70 seconds at all given casting speeds. With increasing the casting speed, the residual stress level in the center increases in all directions (Figure 3). The axial stress increases at the highest rate, and from the smallest component at a speed of 1 mm/s, it turns to the maximum normal stress at a casting speed of 2 mm/s. It is worth mentioning that, as the shear stresses were much smaller compared to normal stresses, the principal stress values and axes were close to the correspondent normal stress components. Radial and circumferential stress components show similar values at all casting speeds in the center of the billet, and they do not change significantly at casting speeds higher than 1.5 mm/s. The circumferential component of stress in the WIZ at the surface (Figure 4) changes very slightly as the casting speed increases from 1 to 1.5 mm/s with a sharp increase on further raising the speed.

The effect of the billet size on the magnitude of residual thermal stresses can be observed in Figures 5 and 6. In the billet with 300-mm diameter, the maximum principal stress appears after 78 seconds in the WIZ and after 347 seconds in the center. For the 400-mm-diameter billet, these times read 160 and 680 seconds,

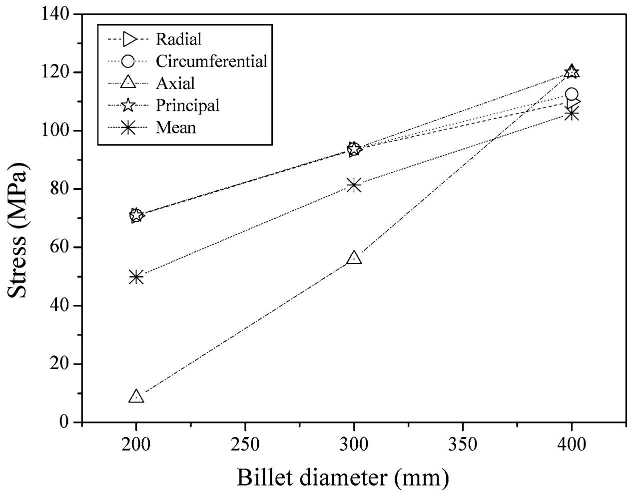

Fig. 5—Effect of billet size on residual stress values formed in the center of the billet at the standard casting speed of 1 mm/s. Radial, circumferential, axial, maximum principal, and mean stresses are reported in this figure.

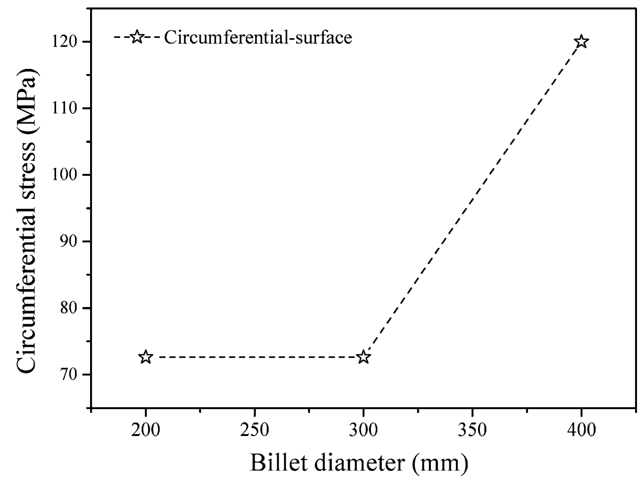

Fig. 6—Circumferential (maximum principal) stress values *vs* billet size in the WIZ at the surface of the billet cast at the speed of 1 mm/s.

respectively. Trends are the same as those observed in Figures 3 and 4, except for the fact that radial and circumferential stress components increase all the way as the billet size increases. Again, the axial stress component increases at the highest rate and becomes the maximum principal stress component in the 400-mm-diameter billet. The circumferential stress (also maximum principal stress) in the WIZ increases dramatically with increasing the billet size and reaches 120 MPa in the 400-mm diameter billet. Another point that can be understood from Figures 3 and 5 is that increasing either the casting speed or the billet size results in the increase of the mean stress in the center of the billets, which in turn increases the failure probability.

IV. CRACKING ASSESSMENT IN THE BILLET

As a good approximation, the grain-refined material under discussion can be assumed to be homogeneous and isotropic; *i.e.*, in macroscopic view, there is no preferred crack orientation and cracks propagate normal to the maximum principal stress component.[35] Having the plane strain fracture toughness of the material and assuming the ingot as a semi-infinite medium, one can calculate by application of fracture mechanics[19,20,22] the critical crack size that leads to catastrophic brittle fracture.

The first step in such an approach is to locate the points in the billet where the maximum principal stress is the highest. Figure 7(a) shows the changes of the maximum principal stress with time in the billet cast under standard conditions (200-mm diameter and 1-mm/s cast speed) and for similar coordinates, as in Section III, except for the lower midradius point (x: 48 mm, y: 35 mm). Corresponding computer-simulated cooling curves are shown in Figure 7(b). From Figure 7(a), it is obvious that the maximum

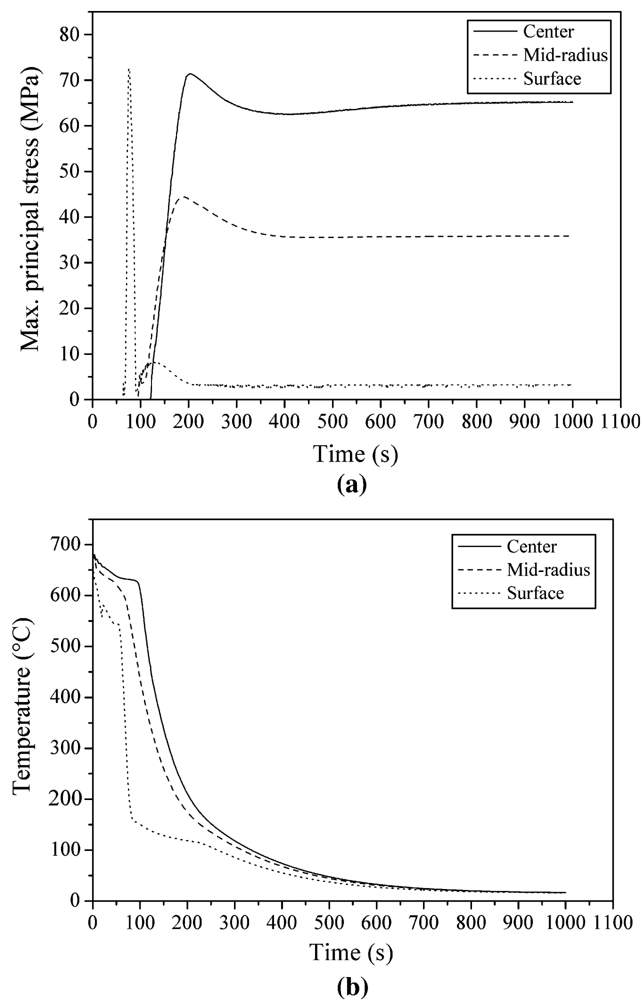

Fig. 7—Computer simulation results showing (*a*) maximum principal stress values for the center (65 mm above the bottom block), midradius (35 mm above the bottom block), and surface (65 mm above the bottom block) of the billet cast under standard casting conditions mentioned in Table I. (*b*) Cooling curves for the points mentioned previously.

principal stress reaches its largest value in the center and in the WIZ, so these two points were used to calculate the critical crack sizes. Maximum principal stress reaches its maximum (73 MPa) after 76 seconds in the WIZ, where the temperature is around 483 K (210 °C) (Figure 7(b)). It falls afterward mainly due to the change in the stress mode at the surface from tensile to compressive.

In the center of the billet, the maximum principal stress reaches its maximum value (71.5 MPa) after 200 seconds at a temperature of 478 K (205 °C) (Figures 7(a) and (b)). When casting reaches the steady state, this value falls and remains constant even after the end of the casting and stopping the water flow.[22] The same trend is observed for the midradius position with the maximum (44 MPa) after 200 seconds and the corresponding temperature of 448 K (175 °C).

As the largest component of the principal stresses reaches its maximum in the center and in the WIZ at the temperature around 473 K (200 °C), the experimentally measured $K_{\mathrm{I}c}$ value (8.29 MPa·m$^{1/2}$[22]) corresponding to this temperature can be applied to assess the critical crack size. Following the same procedure for higher casting speeds and bigger billet sizes, we would be able to investigate the effect of cast speed and billet size on the critical crack size and failure probability of the billets. In accordance with previous works,[19,21,22] cracks with different geometries were assumed to be formed either at the surface or in the center. The penny-shaped crack (PSC) (Figure 8(a)) was chosen for the center and midradius of the billet. The critical crack size for brittle fracture corresponding to this geometry is calculated as follows based on Griffith's analysis:[36]

$$a_c = \frac{\pi}{4}\left(\frac{K_{\mathrm{I}c}}{\sigma}\right)^2 \qquad [1]$$

At the surface of the billet, the surface breaking semicircular (thumbnail) crack (Figure 8(b)) is chosen, for which the critical crack size is related to the $K_{\mathrm{I}c}$ and nominal stress as follows:[36]

$$a_c = \frac{\pi}{(2\times 1.13)^2}\left(\frac{K_{\mathrm{I}c}}{\sigma}\right)^2 \qquad [2]$$

Changes in the critical crack size with casting speed are presented in Figures 9(a) and (b) for the center and the WIZ at the surface of the billet. The critical crack sizes were calculated by applying Eqs. [1] and [2] to the corresponding principal stress values of the center and the WIZ (Figure 7(a)) and the $K_{\mathrm{I}c}$ value at 473 K (200 °C). As can be seen in Figure 9(a), for the penny-shaped crack the critical crack size leading to catastrophic failure decreases with increasing the casting speed. The same trend is observed for the thumbnail crack in the WIZ (Figure 9(b)). The difference is that no changes are observed in the latter case between 1 and 1.5 mm/s casting speeds mainly because no changes occur in the maximum principal stress in this range.

Figures 10(a) and (b) show the effect of billet size on the critical crack size formed in the center and in the WIZ, respectively. Like Figures 9(a) and (b), with increasing the billet size, the critical crack sizes leading to catastrophic failure decrease, resulting in higher cracking susceptibility.

V. DISCUSSION

The main idea behind application of fracture mechanics is that there must be some pre-existing voids, flaws, or cracks at the tip of which the stress level is amplified

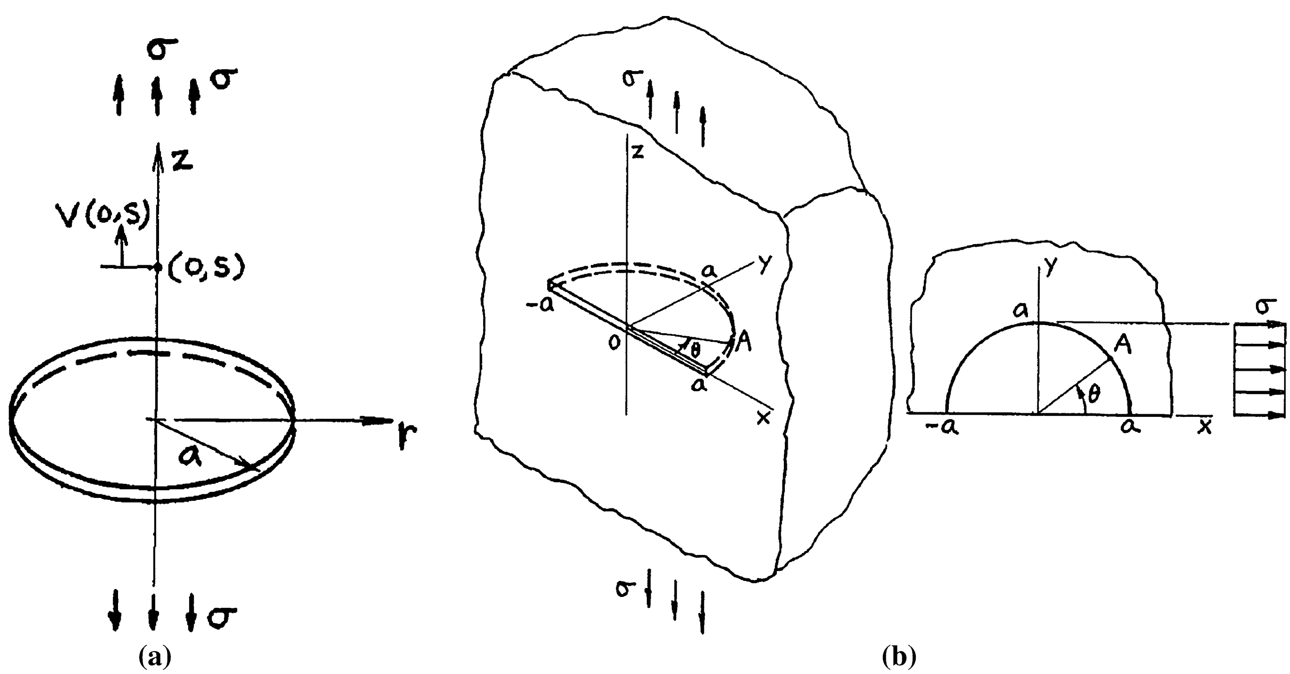

Fig. 8—Schematic view of the crack geometries used in this study. (*a*) A penny-shaped crack. V(0,s) is the displacement at (0,s) when uniform pressure σ is applied on crack surfaces. (*b*) A thumbnail crack in a semi-infinite body ($y \geq 0$) ($y = 0$: free surface).[36]

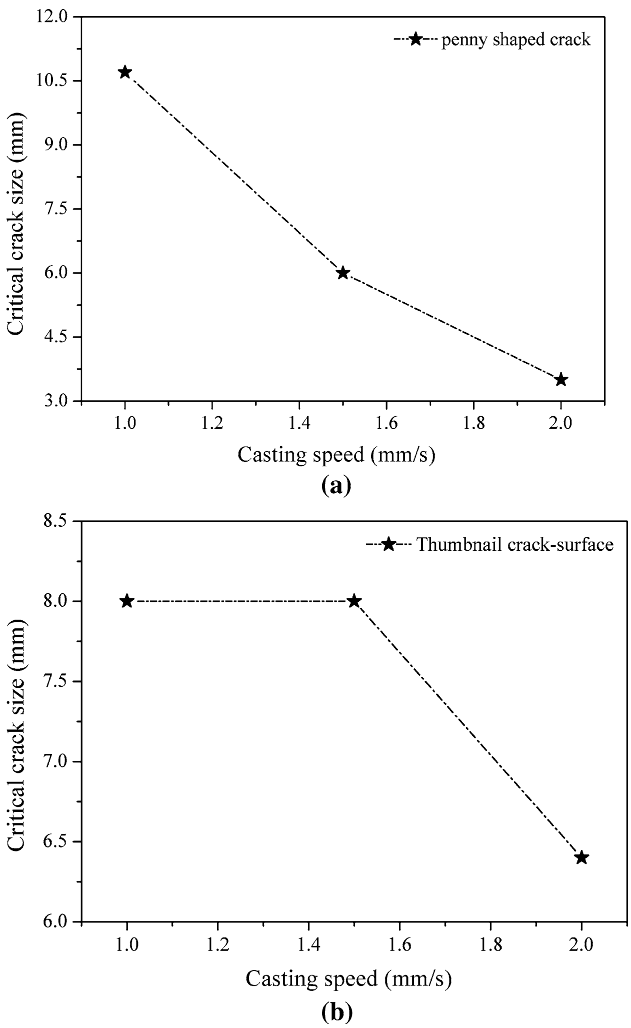

Fig. 9—Critical crack sizes in billets cast at various speeds: (*a*) the penny-shaped crack in the center of the billet and (*b*) the thumbnail surface crack in the WIZ.

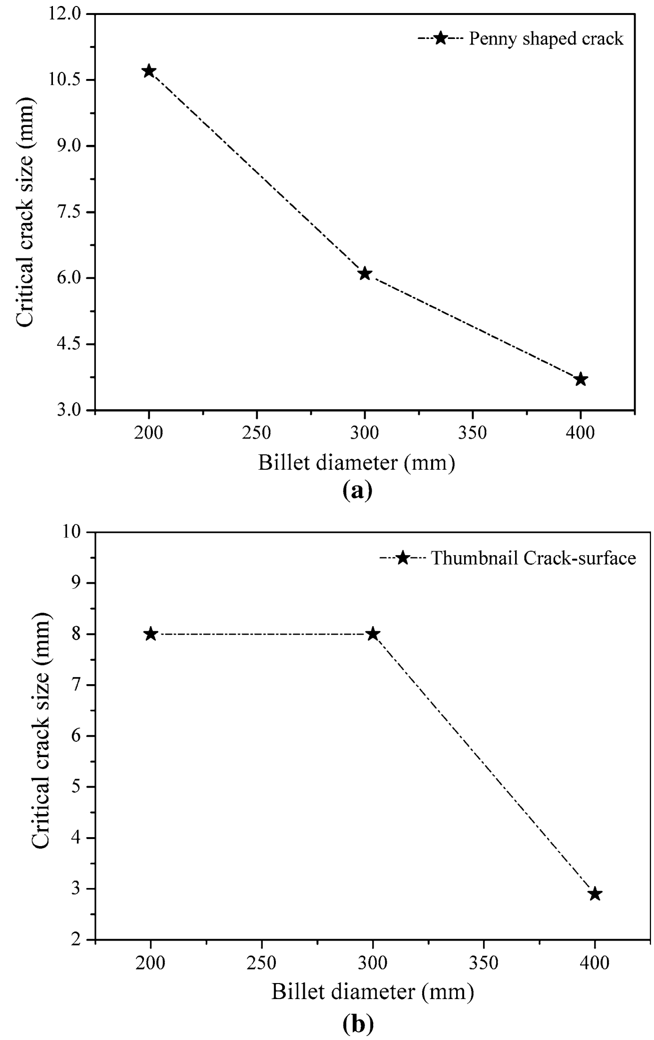

Fig. 10—Critical crack sizes in billets with various diameters: (*a*) the penny-shaped crack in the center of the billet and (*b*) the thumbnail surface crack in the WIZ.

to some critical levels. Such voids might be inclusions, chains of pores, or hot tears that reach a critical size. Cold cracking may also be the continuation of hot tearing; *i.e.*, a hot crack that reaches a critical length and is oriented in the favorable direction might lead to catastrophic failure of the billet and cold cracking. However, there is not much information available on the exact mechanism of cold cracking; therefore, the main assumption is that such defects exist at the onset of cold cracking.

Distribution of residual thermal stresses in the billet (Figure 2) shows that the stress state in the center of the billet is mainly tensile. This holds for almost the whole casting time except for the very beginning, when it is slightly under compression due to the contraction of the surface. At the surface of the billet, stresses are tensile in the WIZ, but they turn to compressive upon further cooling (Figure 7(a)). As cracks are expected to initiate and propagate under tensile load fields, the center of the billet and the WIZ are the most vulnerable locations in the billet to cracking. In round billets, compressive stresses replace the tensile ones at the surface soon after the surface leaves the impingement zone. This results in an acceptable billet, although some small cracks may form in this stage. According to fracture mechanics assessment (Figure 9(b)), microcracks that reach the critical size of 8 mm may propagate catastrophically and result in failure of billets (200-mm diameter, 1 mm/s). This is mainly observed in rectangular flat ingots (slabs) where the stress state in the vicinity of the narrow side remains tensile.[19,37] Under such conditions, large thumbnail cracks may propagate spontaneously in the tensile stress field and result in J cracks. (These cracks have a form similar to the letter "J" that start at the billet surface and go through the billet interior. They suddenly bend afterward and move upward to the head of the billet.)[20,21,38] In the center of the 200-mm billet, the situation becomes critical after 200 seconds when the largest component of principal stresses reaches its maximum value (71.5 MPa for the standard case).

The increase in the magnitude of residual thermal stresses with increasing the casting speed and billet size

(Figures 3 through 6) is related to the increase in heat input. Heat input in the billet is a function of the energy content of the material, *i.e.*, the balance between the heat introduced by the molten metal in the mold, latent heat of fusion, and the heat extracted often by the mold and direct water cooling. The heat input depends on the casting speed and billet size. Faster casting speeds increase the heat input, which in turn results in steeper temperature gradients and more inhomogeneous thermal contractions (Figure 11). Similarly, a larger billet size results in the increased heat input and a longer thermal conduction path. The specific heat of the liquid C_{pl} contributes to only ~5 pct of the total energy content of the material; hence, the melt temperature has low impact on the heat flow and the eventual thermal stresses.[1] The rate of increase of residual thermal stresses is higher in the axial direction compared to the radial and circumferential directions. This can be explained by the fact that because the thermal conductivity of the material changes only slightly, the increased heat input results in a deeper sump, which in turn brings about higher temperature differences in the axial direction (Figure 11). It can also be mathematically shown by using the advection diffusion heat flow equation in cylindrical coordinates:[1]

$$\rho V C_p \frac{\partial T}{\partial z} = k\left(\frac{\partial^2 T}{\partial r^2} + \frac{1}{r}\frac{\partial T}{\partial r} + \frac{\partial^2 T}{\partial z^2}\right) + \rho L V \frac{\partial f_s}{\partial T}\frac{\partial T}{\partial z} \quad [3]$$

where ρ is the density, V is the casting speed, C_p is the specific heat, k is the thermal conductivity, L is the latent heat of fusion, and f_s is the fraction solid (note that the term $\left(\frac{1}{r^2}\frac{\partial^2 T}{\partial \theta^2}\right)$ falls out because of the axial symmetry). The left-hand side is the convective heat flow (input), which increases by increasing the billet size or cast speed. The first compound term on the right is the diffusive heat flow and the second term the latent heat generation. The numerical solution of Eq. [3] in the steady-state condition has shown that the sump depth increases with the square of the diameter, linearly with the cast speed, and is inversely proportional to the alloy thermal conductivity,[39] which is in good agreement with earlier analytic approximations.[40]

With increasing convective heat input, the left-hand side of Eq. [3] increases, which results in a higher rate of latent heat generation on the right-hand side. Because the thermal conductivity is constant, the temperature gradients should also increase to satisfy the energy conservation relationship. Higher temperature gradients cause higher thermal stresses[41] especially in the axial direction (Figures 3 and 5). The fact that higher temperature gradients and subsequently higher stresses are formed in the axial direction can be explained by the cooling conditions during DC casting. Heat extraction during the steady state of the DC-casting process occurs mainly along the radial and circumferential directions. Except for the start-up phase, where the heat is extracted through the bottom block, mold, and water jet, in the steady-state regime, the heat transfers more efficiently along radial and circumferential directions. Heat extraction efficiency in the z direction decreases as the cast length increases. At this stage, the bottom block acts mainly as a billet support.

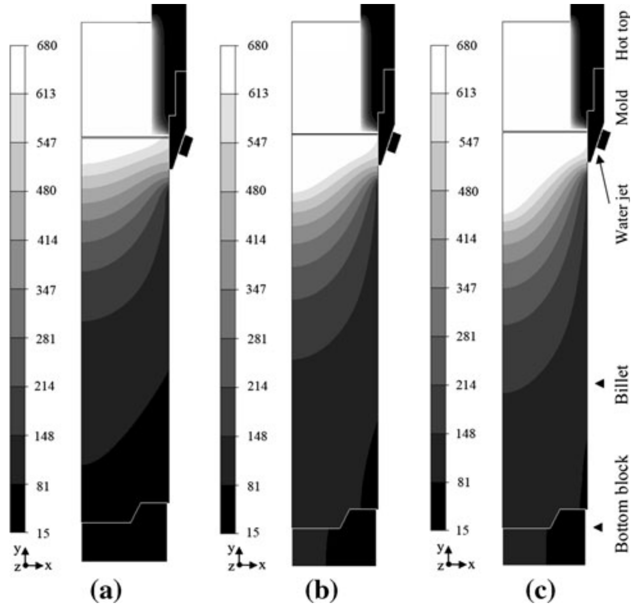

Fig. 11—Computer simulation results showing the temperature contours in DC-cast billets with 200-mm diameter cast at various speeds: (*a*) 1 mm/s, (*b*) 1.5 mm/s, and (*c*) 2 mm/s. Temperatures are in degrees Celsius.

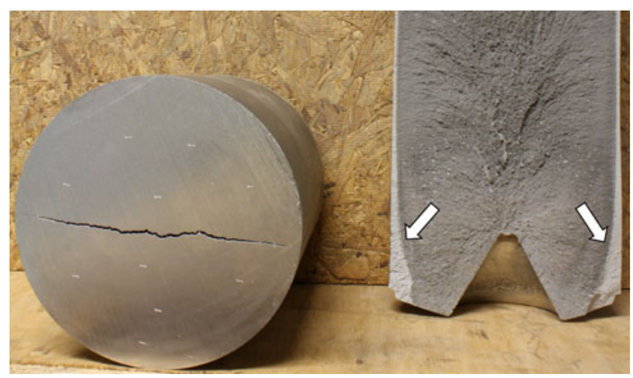

Fig. 12—Photo showing cold cracks in 200-mm 7475 DC-cast billets. Right: view of the billet split open, showing two parts of fracture surface separated by a color contrast; and left: cross section of a similar billet with a cold crack along the radial direction.

The higher residual thermal stresses bring about the lower critical crack size and the higher probability of failure in the billets specifically in the center and in the WIZ (Figure 7(a)). The maximum principal stress at lower casting speeds and smaller billet sizes is oriented either in the radial or circumferential direction, which results in cracks with planes parallel to the axial direction of the billet (Figure 12).[10,22] With increasing the casting speed or the billet size, however, the maximum principal stress turns toward the axial direction of the billet (Figures 3 and 5). This means that the plane of the crack should also turn up to 90 deg to become normal to the maximum principal stress component, which is now parallel to the axial direction of the billet. This results in the so-called cup and cone cracks with various depths depending on the degree of inadequate cooling balance.[10] In our case, when the penny-shaped crack is considered, the plane of the crack is parallel to the axial direction of the billet when the maximum principal stress is oriented in the radial or circumferential direction. When the maximum principal stress aligns with the axial direction of the billet, however, the normal vector of the crack plane has an angle between 0 and 90 deg with the upward axial direction. Similar discussion may be done for the WIZ at the surface of the billet, *i.e.*, with increasing either the casting speed or the billet size, temperature gradients become steeper and higher thermal stresses appear.

Another point that can be understood from Figure 7(a) is that in the steady-state regime, stresses increase in magnitude and reach a maximum. They fall afterward a little bit and reach a plateau, which remains constant up to the end of casting. This is also the case for the newly created elements afterward, and the stresses that reach the plateau value retain their magnitude until the billet is annealed or sawn.[20,22]

In the range of water flow rates chosen in this research, our results are in agreement with the experimental results reported by Matsuda *et al.*,[10] *i.e.*, no impact on cracking susceptibility. At higher water flow rates (130 to 310 L/min), however, cracking occurred in practice.[10] Regarding the water temperature, the experimental results show that the heat flux decreases slightly as the water temperature increases.[42] In the water temperature range of 288 K (15 °C) to 318 K (45 °C), however, these changes are not considerable and may explain the negligible effect of water temperature on the simulation results.

VI. CONCLUDING REMARKS

The effect of various casting variables was studied in order to determine the cracking susceptibility in DC-cast billets. Thermomechanical simulations revealed that at the constant casting speed and billet size, the water temperature, water flow rate, and melt temperature have negligible impact on either the magnitude or the distribution of residual thermal stresses. Casting speed and billet size, however, appeared to be the most influential variables. Increasing either the casting speed or the billet size resulted in increased temperature gradients and, consequently, higher thermal stresses not only in the center but also in the WIZ. The thermal stress in the axial direction of the billet increases faster than the radial and circumferential directions with the increasing casting speed and billet diameter. As a result, the maximum principal stress axis rotates toward the billet axis with changing the process parameters. As cracks preferably align and propagate normal to the maximum principal stress component, the rotation of the maximum principal stress axis results in different crack plane orientations to be formed during DC casting. At lower casting speeds and billet sizes, the maximum principal stress component lies either along the radial or circumferential direction, leading to cold cracks parallel to the axial direction. At higher cast speeds or larger billet diameters, however, the normal vector of the crack planes tilts and becomes aligned normal to the maximum principal stress, which is in the axial direction and results in cup and cone cracks.

ACKNOWLEDGMENTS

This research was carried out under Project No. MC4.05237 in the framework of the Research Program of the Materials innovation institute (www.m2i.nl). Support and fruitful discussions with Dr. W. Boender (Corus R&D) are appreciated. Another important basis of the present article is given by comments received from Messrs D. Mortensen and H. Fjær. The authors especially thank Dr. A. Ten Cate for the preparation of the geometry and mesh simulation files and comments. Remarks offered by Dr. M. Jansen in interpreting the failure mechanisms are also appreciated.

REFERENCES

1. J.F. Grandfield and P.T. McGlade: *Mater. Forum*, 1996, vol. 20, pp. 29–51.
2. U. Chandra and A. Ahmed: in *Modeling for Casting and Solidification Processing*, K.-O. Yu, ed., Marcel Dekker Inc., New York, 2002, pp. 55–93.
3. J.R. Davis: *Aluminium and Aluminium Alloys, ASM Speciality Handbook*, ASM INTERNATIONAL, Materials Park, OH, 1994, pp. 68–69.
4. M. Lalpoor, D.G. Eskin, and L. Katgerman: *Mater. Sci. Eng., A*, 2008, vol. 497, pp. 186–94.
5. J.B. Hess: *Metall. Trans. A*, 1983, vol. 14A, pp. 323–27.
6. B. Hannart, F. Cialti, and R. Van Schalkwijk: in *Light Metals 1994*, U. Mannweiler, ed., TMS, Warrendale, PA, 1994, pp. 879–87.
7. Z. Yubo, C. Jianzhong, Z. Zhihao, Z. Haitao, and Q. Ke: *Mater. Sci. Eng., A*, 2005, vol. 406, pp. 286–92.
8. W. Roth: *Z. Metallkd*, 1949, vol. 40 (12), p. 145.
9. B. Commet, P. Delaire, J. Rabenberg, and J. Storm: in *Light Metals*, P.N. Crepeau, ed., TMS, Warrendale, PA, 2003, pp. 711–17.
10. K. Matsuda, S. Nagai, Y. Miyate, H. Maehara, and I. Tsukuda: *6th Int. Aluminum Extrusion Technology Seminar*, Aluminium Association and Aluminium Extruder's Council, Chicago, IL, 1996, vol. I, pp. 525–28.
11. A. Burghardt, B. Commet, J.-M. Drezet, and H.G. Fjær: in *Modeling of Casting, Welding and Advanced Solidification Processes IX*, P.R. Sahm, P.N. Hansen, and J.G. Conley, eds., Shaker Verlag, Aachen, Germany, 2000, pp. 25–32.
12. W. Schneider, E.K. Jensen, and B. Carrupt: in *Light Metals*, J. Evans, ed., TMS, Warrendale, PA, 1995, pp. 961–67.
13. S. Benum, D. Mortensen, H. Fjær, H.-G. Øverlie, and O. Reiso: *Light Metals*, 2002, W. Schneider, ed., TMS, Warrendale, PA, 2002, pp. 967–74.
14. J.L. Dassel and T.C. Zinniger: in *Light Metals*, TMS-AIME, Warrendale, PA, 1982, pp. 793–801.
15. US Patent No. US2007/0102136 A1, 2007.
16. K.-M. Chang and B. Kang: *J. Chin. Inst. Eng.*, 1999, vol. 22, pp. 27–42.
17. J.M. Drezet and M. Rappaz: in *Light Metals*, J. Evans, ed., TMS, Warrendale, PA, 1995, pp. 941–50.
18. H.G. Fjær and A. Mo: *Metall. Trans. B*, 1990, vol. 21B, pp. 1049–61.

19. W. Boender, A. Burghardt, E.P. van Klaveren, and J. Rabenberg: in *Light Metals*, A.T. Tabereaux, ed., TMS, Warrendale, PA, 2004, pp. 679–84.
20. O. Ludwig, J.-M. Drezet, B. Commet, and B. Heinrich: in *Modeling of Casting, Welding and Advanced Solidification Processes XI*, C.-A. Gandin and M. Bellet, eds., TMS, Warrendale, PA, 2006, pp. 185–92.
21. W. Boender and A. Burghardt: *Proc. 5th Decennial Int. Conf. on Solidification Processing*, H. Jones, ed., University of Sheffield, Sheffield, United Kingdom, 2007, pp. 714–18.
22. M. Lalpoor, D.G. Eskin, and L. Katgerman: *Metall. Mater. Trans. A*, 2009, vol. 40A, pp. 3304–13.
23. E.E. Madsen and G.E. Fladmark: in *Numerical Solution of Partial Differential Equations*, G.E. Fladmark and J.G. Gram, eds., D. Reidel Publishing Company, Dordrecht, The Netherlands, 1973, pp. 223–40.
24. E.E. Madsen: in *Numerical Methods in Thermal Problems*, R.W. Lewis and K. Morgan, eds., Pineridge Press Limited, Swansea, United Kingdom, 1979, pp. 81–89.
25. H. Fossheim and E.E. Madsen: in *Light Metals*, W.S. Peterson, ed., TMS-AIME, Warrendale, PA, 1979, pp. 695–720.
26. E.K. Jensen and W. Schneider: in *Light Metals*, C.M. Bickert, ed., TMS-AIME, Warrendale, PA, 1990, pp. 937–43.
27. D. Mortensen: *Metall. Mater. Trans. B*, 1999, vol. 30B, pp. 119–33.
28. M. Lalpoor, D.G. Eskin, and L. Katgerman: *Proc. 12th Int. Conf. on Fracture*, Ottawa, 2009, National Research Council of Canada, Ottawa, Canada, 2009 (CD).
29. B. Magnin, L. Katgerman, and B. Hannart: in *Modeling of Casting, Welding and Advanced Solidification Processes VII*, M. Cross and J. Campbell, eds., TMS, Warrendale, PA, 1995, pp. 303–10.
30. O. Ludwig, B. Commet, J.-M. Drezet, C.L. Martin, and M. Suery: in *Modeling of Casting, Welding and Advanced Solidification Processes X*, D.M. Stefanescu, J. Warren, M. Jolly, and M. Krane, eds., TMS, Warrendale, PA, 2003, pp. 183–90.
31. M. M'Hamdi, A. Mo, and H.G. Fjær: *Metall. Mater. Trans. A*, 2006, vol. 37A, pp. 3069–83.
32. D.G. Eskin, Suyitno, J.F. Mooney, and L. Katgerman: *Metall. Mater. Trans. A,* 2004, vol. 35A, pp. 1325–35.
33. O. Ludwig, J.-M. Drezet, C.L. Martin, and M. Suéry: *Metall. Mater. Trans. A*, 2005, vol. 36A, pp. 1525–35.
34. M. Lalpoor, D.G. Eskin, and L. Katgerman: *Proc. THERMEC 2009, Adv. Mater. Res.*, 2010, vols. 89–91, pp. 319–24.
35. M. Schöllmann, H.A. Richard, G. Kullmer, and M. Fulland: *Int. J. Fract.*, 2002, vol. 117, pp. 129–41.
36. H. Tada, P.C. Paris, and G.R. Irwin: *The Stress Analysis of Cracks Handbook*, 3rd ed., ASME, New York, NY, 2000, pp. 342 and 410.
37. V.A. Livanov: in *Aluminum Alloys*, A.F. Belov and G.D. Agarkov, eds., Oborongiz, Moscow, 1955, pp. 128–68.
38. R.K. Paramatmuni, K.-M. Chang, B.S. Kang, and X. Liu: *Mater. Sci. Eng. A*, 2004, vol. 379, pp. 293–301.
39. S.C. Flood, P.A. Davidson, and S. Rogers: in *Modeling of Casting, Welding and Advanced Solidification Processes VII*, M. Cross and J. Campbell, eds., London, 1995, pp. 801–08.
40. V.I. Dobatkin: *Continuous Casting and Casting Properties of Alloys*, Moscow, Oborongiz, 1948.
41. N. Noda, R.B. Hetnarski, and Y. Tanigawa: *Thermal Stresses*, 2nd ed., Taylor & Francis, New York, NY, 2003, pp. 221–93.
42. J. Langlais, T. Bourgeois, Y. Caron, G. Beland, and D. Bernard: in *Light Metals*, J. Evans, ed., TMS, Warrendale, PA, 1995, pp. 979–86.